FOI

Dual Frequency Sonar - pre study and field experiment

MATTIAS JÖNSSON, ALEX CEDERHOLM, ÖRJAN STAAF,
BRODD LEIF ANDERSSON, PER SÖDERBERG, JÖRGEN PIHL

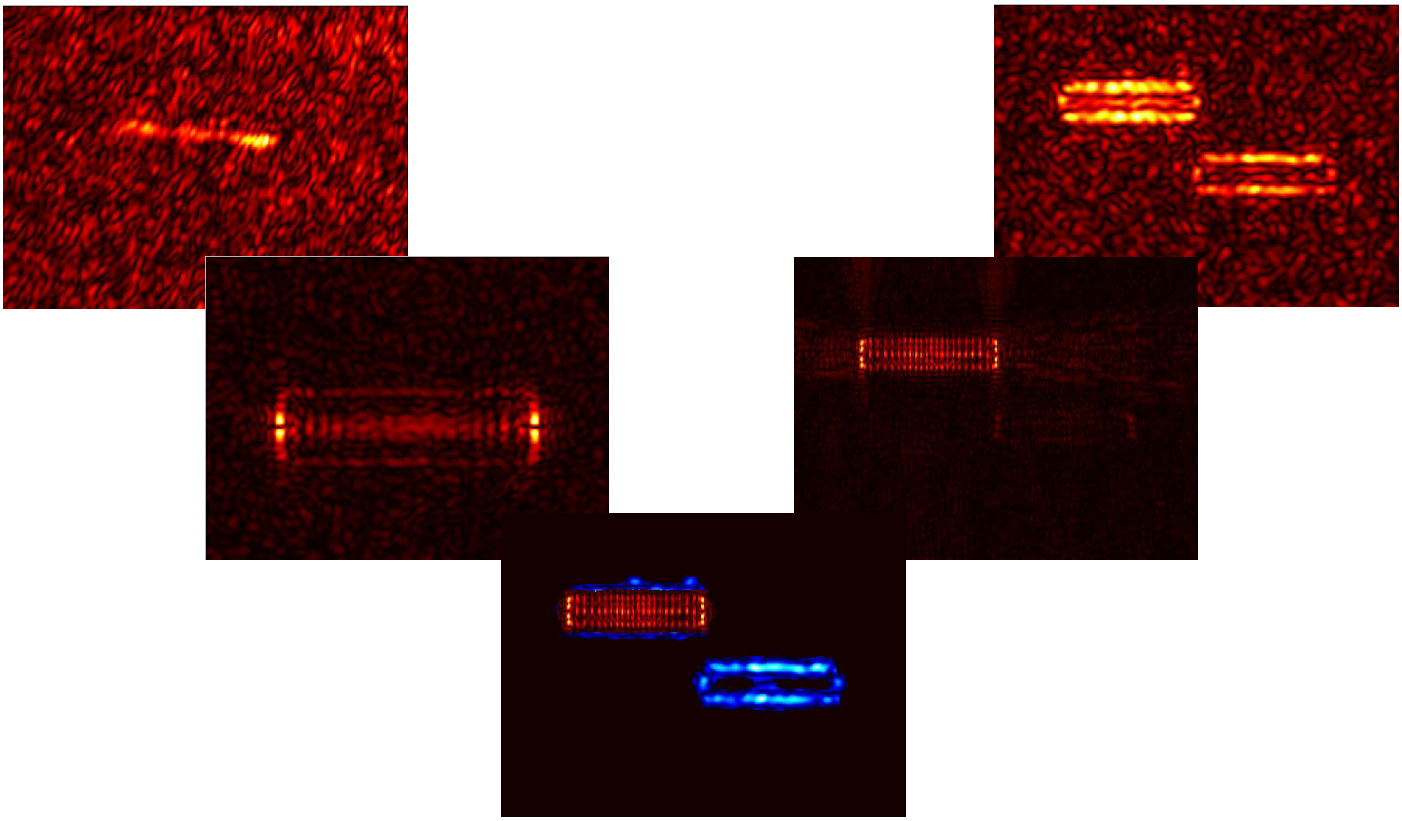

FOI-R--2666--SE Technical report
ISSN 1650-1942 January 2009

Defence & Security, Systems and Technology

MATTIAS JÖNSSON, ALEX CEDERHOLM,
ÖRJAN STAAF, BRODD LEIF ANDERSSON,
PER SÖDERBERG, JÖRGEN PIHL

Dual Frequency Sonar - pre study and field experiment

Titel	Dubbelfrekvenssonar – förstudie och fältförsök
Title	Dual Frequency Sonar – pre study and field experiment
Rapportnr/Report no	FOI-R--2666--SE
Rapporttyp Report Type	Teknisk rapport Technical report
Sidor/Pages	48p
Månad/Month	Januari/January
Utgivningsår/Year	2009
ISSN	ISSN 1650-1942
Kund/Customer	Försvarsmakten
Forskningsområde Programme area	4. Sensorer och signaturanpassning 4. Sensors and Low Observables
Delområde Subcategory	43 UV-teknik – sensorer 43 Underwater Technology - Surveillance, Target acquisition and Reconnaissance
Projektnr/Project no	E20607
Godkänd av/Approved by	Helena Bergman

FOI, Totalförsvarets Forskningsinstitut
Avdelningen för Försvars- och säkerhetssystem

164 90 Stockholm

FOI, Swedish Defence Research Agency
Defence & Security, Systems and Technology

SE-164 90 Stockholm

Sammanfattning

Med ambitionen att förbättra framtida MCM-operationer har en dubbelfrekvenssonar studerats genom simuleringar och experiment. Hypotesen att begravda objekt endast kommer att vara synliga för lågfrekvent SAS, och att ytliggande objekt kommer att vara synliga för både hög- och lågfrekvent SAS testades. För att simulera dubbelfrekvent SAS utvecklades en strålgångsmodell. Simuleringarna antydde att den reflekterade energin från begravda objekt reducerades när centrumfrekvensen ökade. Dessutom visade det sig att SAS-bilder bevarade de huvudsakliga strukturerna när jämförelse gjordes med resultat från fullfältsmodellering och fältförsök. Experimentellt testades en ny mottagarantenn för lågfrekvent SAS och en sidtittande sonar för högfrekvensavbildning vid den rälsbaserade SAS-försöksstationen i Djupviken. Testexperimenten visade att den nya utrustningen fungerade. Objekt identifierades både med hjälp av lågfrekvent SAS och sidtittande högfrekvent sonar. Signalbehandlingskod för detektion och separation av ytliggande och begravda objekt implementerades och testades på både simulerade och experimentella SAS-bilder. Begravda objekt segmenterades och separerades från ytliggande objekt genom signalbehandlingen.

Nyckelord: Motmedel Minor, Dubbelfrekvenssonar, Syntestisk Apertur Sonar (SAS), Sidtittande Sonar, Begravda Objekt, Strålgångsmodell, Detektion

Summary

With the ambition to improve future MCM operations the dual frequency sonar was studied by simulations and experiments. The hypothesis that buried objects will be visible to low frequency SAS only, while proud objects are visible to both low and high frequency SAS was tested. A ray tracing model was developed for simulating a dual frequency SAS. This model indicated that the reflected energy from buried targets was reduced when the center frequency was increased. In addition, SAS images indicated that the major structures were not lost when comparing with results from full-field modeling and field data processing. In the experiments a new receiver array for low frequency SAS and a sidescan sonar for high frequency imaging were deployed and tested at the rail based SAS facility in Djupviken. The test experiments indicated that the new equipment was working as expected. Objects were identified using both the low frequency SAS and the high frequency sidescan sonar. Signal processing code for detection and separation of proud and buried objects was implemented and tested on both simulated and experimental SAS images. Buried objects were segmented and separated from proud object using the dual frequency processing.

Keywords: Mine Counter Measure (MCM), Dual Frequency Sonar, Synthetic Aperture Sonar (SAS), Sidescan Sonar, Buried Objects, Ray Tracing Model, Detection

Contents

1 Introduction

Merchant shipping is by far the largest carrier of freights in the world. Concerning Sweden, just to take an example, more than 95 % [1] of imported and exported goods are carried by transports. Coastal harbors are therefore very important locations in both national and international conflicts. One way to effectively block a harbor is the use of sea-mines or even just the threat to use them. In such a context, the Royal Swedish Navy (RSwN) may very likely be asked to secure a harbor during a peace-keeping operation abroad. Besides securing civilian economical interests the Navy should support land based operations as well. The ability to deploy or evacuate military personnel and equipment requires maritime mobility in costal areas. The best counteract to a mining operation is a fast and accurate Mine Counter Measure (MCM) operation. In the Baltic Sea there is a large amount of mines and explosives from earlier wars and the sea was also used for dumping such hazardous material in the past. This kind of materials also affects fishing, sea-prospecting and -communications. More important when larger civilian projects are planned a mine inspection might be necessary. The RSwN continuously performs MCM operations in the Baltic Sea.

Today MCM operations are carried out using hull mounted sonars or towed sidescan sonar. The mine hunting vessel scans the designated area in several parallel tracks imaging the bottom. When an object is detected a Remotely Operated Vehicle (ROV) armed with a sonar and video camera is used to classify and identify the detected target. This operation is time consuming. At present the RSwN has no operational ability to detect an object buried in the sea bottom.

Sonar systems, particularly side-looking sonar systems, are adapted for detecting naval mines lying on, or moored just above the sea bed. Mine detection becomes more difficult, and in some cases impossible, when the mine is buried in the sea bottom. Naval mines may be buried by various methods both active and inactive depending on environmental conditions. There are mines that have the ability to bury them selves by pumping and eject streaming water through mouthpieces in intervals back and forth. This undulating movement will bury the mine. Other possibilities for buried mines are that the ongoing sedimentation will cover the mine, or that the sediment is muddy and the object will sink into it and cover the mine completely.

Detection of buried objects is complicated due to the frequency dependent attenuation in the seabed and incident angle dependent reflections at the water-bottom interface. For buried mines the frequency should be low and the incident angle high. A low frequency downlooking sonar is however time-consuming and impropriate for mine-hunting. The MCM personal risk is decreased if they are kept outside the minefield. Therefore unmanned platforms like ROVs and Autonomous Underwater Vehicles (AUV) are useful. Hence there has been a rapid development of new sensors adapted to these carriers, in particular the development of Synthetic Aperture Sonar (SAS).

1.1 Review

For detection of targets resting on the sea bottom there are commercial SAS systems available today, producing images with high resolution, as for instance described by Lövgren [2] and Hansen et al. [3]. An important aspect closely linked to MCM is the mine burial process, which is emphasized by the special

issue of the IEEE Journal of Oceanic Engineering [4], with a historical review and an introduction of the field found in [5]. To detect buried targets a hull-mounted down-looking 5 kHz parametric sonar can be used. A field experiment was presented by Morén and Pihl [6], where a buried concrete disk at a depth of about 0.4 m in the sediment was detected. A ROV experiment was conducted by Ivansson et. al. [7] to overcome difficulties in positioning the vehicle at the desired position. A dense grid of profiles revealed the previously mentioned concrete disk and its size. Morén et. al. [8] described a field experiment aimed at demonstrating methods for localization and classification of objects buried in the sea bottom. Among the configurations was a bistatic ROV experiment illuminating a semi-buried ammunition box. The experiment was analyzed by Karasalo and Skogqvist [9]. Using a fast approximate Ray-Kirchoff model an estimation of the position, the rotation and the material properties of the semi-buried ammunition box was performed using a stepwise inversion scheme.

To achieve high resolution sidescan images of buried objects despite the low frequency required for penetration parametric sonars, SAS systems or a combination of both have been suggested. Pinto et al. [10] describe parametric sidescan sonar and spotlight parametric SAS experiments for detection and classification of buried objects. Piper et al. [11] present detections of buried targets using a 20 kHz SAS system. The effect of penetration below the critical angel due to seabed ripples is discussed. Dugelay et al. [12] studies issues crucial to the detection of buried objects using parametric SAS. Parametric sonar generation, Signal-to-Noise Ratio (SNR) for different sediment types and difference in SAS focusing compared to proud targets are investigated. The results include that the narrow parametric beam requires spotlight mode SAS, and a conventional low-frequency SAS will not suffer from the high loss of energy during the parametric effect. Belkacem et al. [13] suggest a down looking planar SAS system where the synthetic aperture processing is performed in two directions producing a three dimensional representation of the scanned volume. The method is shown on data from a scaled tank experiment. Furthermore the defocusing of buried objects when the bottom sound speed is unknown is analyzed. Accurate positioning is important for SAS processing. Cutrona [14] states a required accuracy of $1/8^{\,th}$ of a wavelength. To facilitate controlled SAS experiments with high positioning accuracy, a rail based SAS system was described by Jönsson and Staaf [15]. A couple of Mine-Like Objects (MLO) were buried in the area of the rail. Jönsson [16] conducted a preliminary analysis from a field experiment using the rail SAS system. Further results were reported by Jönsson et. al [17], together with results from a parametric down-looking sonar survey in the target area.

Down-looking ROV experiments on the buried disk using higher frequencies, 10 and 20 kHz, was conducted at the test site and reported by Ivansson et. al. [18]. Surprisingly the highest frequency 20 kHz, achieved the highest target to bottom echo ratio. This was explained theoretically by a slowly varying transition layer between the water and the sediment. Obviously the selected frequency should depend on the geoacoustic parameters. Staaf [19] describes a field experiment designed to measure bottom penetration as a function of incident angle and frequency. Furthermore, a setup designed to measure the important geoacoustic parameters was also described.

The issue of separation of buried and proud objects has received some interest. Zakharia et al. [20] describes a parametric SAS system with dual frequency receivers, where three images can be obtained simultaneously, two high frequency images using the primary frequencies and one low frequency image using the secondary frequency. Gough et. al. [21] compares SAS images of the seabed using different frequencies with the ambition to separate buried

objects from proud objects. This is studied using both simulations and experimental data. Piper and Lim [22] presents an AUV based dual frequency SAS system. Field experiments show a buried 7.5×35 cm cylinder visible in the low-frequency image but not in the high-frequency image.

Targets has to be detected and classified from the large amount of high resolution SAS images produced by a SAS on an AUV. Efforts towards an automated system have to be taken. In [23], Maussang et al. propose an automated echo detection method for SAS images, where the method is based on statistical properties of images from proud/buried targets including reverberation. A detection-oriented Markov random field model is instead used by Reed et al. [24], which segments sidescan sonar images of proud targets into regions of shadow, sea bottom and object highlight. Objects are then classified by a co-operating statistical snake model and results are given both for synthetic and real images. Moreover Montanardi et al.[25], use a concurrent detection and classification for MCM by AUVs and the system is demonstrated through theory, simulation and field experiments. Here the detection is based on an energy detector and a peak tracking mechanism, followed by a higher order spectral classification process.

An AUV based mine hunting concept study was performed by Cederholm and Jönsson [26] from a signal processing perspective. For imaging of proud objects a 100 kHz SAS system was suggested giving a 2.5×2.5 cm range independent resolution. This is a higher resolution than any real aperture system regardless of frequency can achieve, unless at extremely short ranges. In addition a SAS system also improves the SNR. Improved SNR will decrease the false alarm rate and thus increase MCM operation speed. Both enhanced resolution and SNR will probably improve the classification process. For imaging of buried targets a 25 kHz SAS system was suggested, due to the limited frequency for successful imagery below the sea bottom.

1.2 Current Study

The report should be seen as number two in a trilogy of reports, focusing on MCM operation applied to buried targets. The first report [26] outlines a vision of a future MCM concept. This report gives a progress report of the research activities taken to highlight difficulties and possibilities with the proposed concept. The third report scheduled for next year will give conclusions and recommendations on a higher level. The work includes: the development of a ray tracing model for fast predictions, the deployment and testing of a new receiver array for low frequency SAS, the deployment of a sidescan sonar for high frequency imaging and the implementation of signal processing code for detection and separation of proud and buried objects. In this report attention is turned to the rail based SAS system and buried targets. The concept study in [26] suggest imaging using two different frequency bands for proud and buried objects. Here a dual frequency sonar is considered, combining the vast experience of buried target detection and synthetic aperture processing. The dual frequency sonar consists of two sub-systems, a low frequency SAS system and a high frequency sidescan system. The dual frequency possibilities are studied using simulations and field experiments. The purpose of the current study is to evaluate the proposed concept using simulations and field experiments. The high frequency sidescan sonar and the low frequency SAS will be verified individually and then used together as a dual frequency sonar. Similarly the developed simulation model must be verified against other models before it is used for dual frequency studies.

1.3 Outline

In the Chapter 2, Method, the simulation and the field experiment are described together with the signal processing for detection and separation of buried and proud objects. The results in Chapter 3 then describes the results from verification of the simulation model, the sidescan sonar and the penetration SAS system first separately and then together as a dual frequency sonar. The report then ends with the discussions in Chapter 4, where conclusions are stated and recommendations are given.

2 Method

2.1 Simulation

Computer simulations can support the design of a sonar system by predicting the sonar performance in a particular underwater environment. A first version of a fast ray tracing model [27] for two homogeneous halfspaces (water/sea bed) has been implemented. The ray tracing model, SASRAY, is described in detail in Appendix A. A simulation with an accurate full-field model has been included for reference purpose [28].

Sonar and geometrical settings are adjusted to the experiments considered. A horizontal uniform linear array is used with 16 elements and one wavelength spacing adjusted to the sound velocity 1500 m/s and the center frequency 30 kHz. The source pulse transmitted at each ping is a Linear Frequency Modulated (LFM) pulse with center frequency 25 kHz, bandwidth 10 kHz and pulse length 20 ms. All simulated signals is sampled with a frequency of 200 kHz. The array is moving in line with a straight track of length 12.8 m with a movement of 0.4 m between each ping, resulting in 33 pings for every SAS simulation. Referring to Figure A.2, the geometrical configurations is set to $d_1 = 6$ m in vertical distance between the straight array track and the bottom and $d_2 = 0.5$ m in vertical distance between the bottom and the center of the target. The horizontal and perpendicular distance between the midpoint of the straight track and the center of the target is set to 25 m, cf. $l = l_1 + l_2$ in Figure A.2. Four types of simulations are included.

(S.1) The first simulation setup is intended to verify that the SASRAY model is capable of simulating different target configurations used in the field experiment. Simulations are carried out for three different generic targets. The targets are: A sphere with radius 0.25 m, a quadratic box with sides 0.5 m and a cylinder with length 1.89 m and radius 0.325 m. In particular the cylinder models the target used in the field experiment composed of car tires mounted on an axle, and it is also modeled when buried and bottom scatters are present.

(S.2) In the second simulation setup the full-field model is used for comparison to SASRAY.

(S.3) The third simulation setup is designed to indicate how the response of a buried target depends on frequency. The idea is to use low frequency SAS to detect buried objects, while using high frequency SAS to discriminate proud objects. Thus, a buried target will be more visible to a low frequency sonar than a high frequency sonar. This setup will also indicate if the targets already buried at the field experiment site is useable. A high frequency mode is suggested as follows. A horizontal uniform linear array is used with 48 elements and one wavelength spacing adjusted to the sound velocity 1500 m/s and the center frequency 100 kHz. The source pulse transmitted at each ping is a LFM pulse with center frequency 100 kHz, bandwidth 30 kHz and pulse length 20 ms. All simulated signals are sampled with a frequency of 200 kHz. Two point scatterers are utilized keeping the remaining SASRAY parameter settings. One scatterer is positioned in the water halfspace 0.5 m above the bottom surface and one scatterer is positioned in the bottom halfspace 0.5 m below the bottom surface.

(S.4) The fourth simulation setup is intended for signal processing evaluation of the dual frequency sonar. Two cylinder objects are positioned above and below the seabed respectively. A low and a high frequency SAS are then

simulated.

2.2 Field Experiment

A new receiver array for low frequency SAS is deployed and tested at the railbased SAS facility in Djupviken. Furthermore a Side Looking Sonar (SLS) for high frequency imaging is also deployed. The equipment is intended to verify the hypothesis that buried objects can be separated from proud objects as they will become invisible to the high frequency sonar in contrast to the proud objects visible to both sonars. In fact, a high frequency SAS would be a better choice than an ordinary SLS, but the resources did not permit such a configuration. However, the principle how to discriminate between buried and proud objects can yet be demonstrated. With the new low frequency receiver array, the field experiment is also intended to improve the detection of the previously buried MLOs last reported in [17]. The equipment is described in detail in Appendix C. Furthermore Appendix D gives a description of the Djupviken test site.

In the experimental area outside the rail the bottom topography is relatively flat. The water depth ranges smoothly from 10 m at the rail to about 12 m where the test objects or targets are located. Three test objects are buried at distances 10-40 m outside the rail. The first object, called the Large Cylindrical Object (LCO) is a 1.8 m long cylinder, made of nine car wheels buried about 10 m from the rail. The two other objects are MLOs of different size; a small one, SMLO, buried about 20 m from the rail and a large one, LMLO, buried at a range of about 40 m from the rail. All objects are buried very shallow with their uppermost parts some 10 cm below bottom, Figure 2.1.

Figure 2.1: From left the LCO, the SMLO and the LMLO.

Another triple of test objects were laid on the sea bottom surface. These targets were made of a special type of concrete called Expanded PolyStyrene (EPS) concrete. EPS concrete is a mixture of polystyrene particles of a few mm in diameter and cement and is normally used in the building industry as a complementary add-on layer to constructions in order to increase heat insulation and sound absorption. The three EPS targets are a truncated cone, a sphere and a brick. All these targets are of about half a meter in size. Since EPS concrete has a lower density than water, weights are attached to all three the targets to submerge them into the water. The sphere has a plastic coating and the truncated cone is provided with a thin sheet metal on its envelope surface. Reflected energy from the targets might emanate from both the targets themselves and the attached weights. The three targets made of EPS concrete are shown in Figure 2.2.

Figure 2.2: From left the truncated cone, the sphere and the brick.

A further set of bottom laid objects are a stone, a ladder and a plate on a stand shown in Figure 2.3. Two of the targets are metallic and of larger size than the EPS targets. The ladder is 3.1 m long and the stand is of one meter size. The stone is maximally half a meter in size but attached to a steel plate which might contribute to the target strength.

Figure 2.3: From left the stone, the ladder and the plate on a stand.

A sketch containing all the targets are shown in figure 2.4. Buried targets are identified by a red circle while the first and second set of bottom located targets is marked by blue and green respectively.

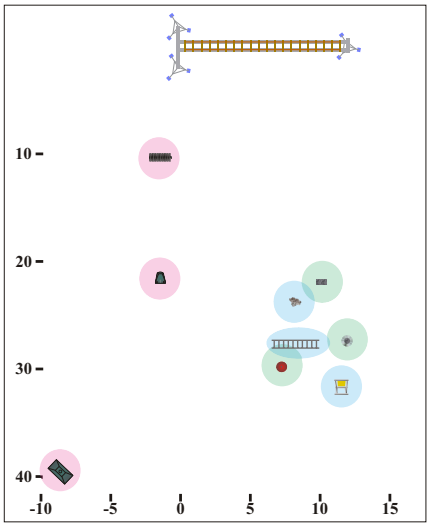

Figure 2.4: Targets used in the field experiment. Buried targets are identified by a red circle while the first and second set of bottom located targets is marked by blue and green respectively.

2.2.1 Experimental Set-up

A series of test experiments (T.1-T.4) is conducted to investigate that the low frequency SAS equipment is working properly. The test experiments are carried out at the FOI tank laboratory and at the field experiment test site. The results are validated against SASRAY simulations.

(T.1) In the first test experiment the transmitter is placed about 3 m in front of the receiver array in the tank laboratory. A 20 ms LFM pulse at 20-30 kHz is emitted and sampled with 200 kHz. This test will verify that desired signal is correctly transmitted and received.

(T.2) The second test experiment is designed to verify that the equipment is working properly mounted together as a SLS. A corner reflector is placed about 3 m in front of the sonar in the tank laboratory. A 20 ms LFM pulse at 20-30 kHz is emitted and sampled with 200 kHz.

(T.3) The third test experiment is carried out at the test site. The sonar is mounted on the wagon and placed on the rail. A corner reflector is positioned about 10 m in front of the rail in the middle of the water column. A 20 ms LFM pulse at 20-30 kHz is emitted and sampled with 200 kHz. This test verifies that the sonar is properly mounted on the carriage.

(T.4) In the fourth and final test experiment the carriage is moved along the rail with the purpose of producing a synthetic aperture. A corner reflector is positioned about 10 m in front of the rail in the middle of the water column. A 20 ms LFM pulse at 20-30 kHz is emitted and sampled with 200 kHz from 33 positions. The carriage is moved to the proper position and the pulse is transmitted. The carriage is then moved half a receiver length, 0.4 m, where a new pulse is transmitted. The procedure is repeated until the maximum synthetic aperture of 12.8 m is reached.

The field experiment consists of four different setups of where two (F.1 and F.2) are aimed at improving the detection of the previously buried objects while the other two (F.3 and F.4) are intended to evaluate the dual frequency sonar.

(F.1) In the first setup a corner reflector is placed above each of the two buried MLOs. This setup will determine their position in the rail coordinate system. A 20 ms LFM pulse at 20-30 kHz is emitted and sampled with 200 kHz from 33 positions. The carriage is moved to the proper position and the pulse is transmitted. The carriage is then moved half a receiver length, 0.4 m, where a new pulse is transmitted. The procedure is repeated until the maximum synthetic aperture of 12.8 m is reached.

(F.2) In the second setup the corner reflectors are removed allowing images of the expected MLO without interfering corner reflectors. A 20 ms LFM pulse at 20-30 kHz is emitted and sampled with 200 kHz from 33 positions. The carriage is moved to the proper position and the pulse is transmitted. The carriage is then moved half a receiver length, 0.4 m, where a new pulse is transmitted. The procedure is repeated until the maximum synthetic aperture of 12.8 m is reached.

(F.3) The third setup is intended for imaging of a scene containing both buried and proud objects allowing the dual frequency sonar performance to be determined. Three objects: a box, a truncated cone and a sphere is positioned on the seabed 30-40 m outside the rail. A series of measurements from 33 positions along the rail is conducted. The carriage is moved to the proper position and the low frequency pulse is transmitted. When the pulse is properly recorded a measurement using the high frequency sonar is conducted. The carriage is then moved half a low frequency sonar receiver length, 0.4 m, where new measurements are conducted. The procedure is repeated until the

maximum synthetic aperture of 12.8 m is reached.

(F.4) The fourth setup is intended for imaging of a scene containing both buried and proud objects allowing the dual frequency sonar performance to be determined. Three objects: a stone, a ladder and an aluminum plate on a stand is positioned on the seabed 30-40 m outside the rail. A series of measurements from 33 positions along the rail is conducted. The carriage is moved to the proper position and the low frequency pulse is transmitted. When the pulse is properly recorded a measurement using the high frequency sonar is conducted. The carriage is then moved half a low frequency sonar receiver length, 0.4 m, where new measurements are conducted. The procedure is repeated until the maximum synthetic aperture of 12.8 m is reached.

2.3 Signal Processing

Signal processing code for detection and separation of proud and buried objects is implemented. The code is a key component in the dual frequency sonar and is intended to be used regardless of whether the sensor signals are simulated or measured. The purpose is to evaluate a detection method described in the literature and extend it to separate buried objects from proud objects.

2.3.1 Detection

Consider the SAS detection algorithm described in [23]. The local mean and standard deviation in a neighborhood of each pixel is computed. Targets are then segmented from the background using a mean and a standard deviation threshold. Let $M(x, y)$ denote a $N_x \times N_y$ SAS image. The local mean, $\mu_M(x_i, y_i)$, and standard deviation, $\sigma_M(x_i, y_i)$, for a pixel (x_i, y_i) is estimated as,

$$\mu_M(x_i, y_i) = \frac{1}{n_x n_y} \sum_{x=-a}^{a} \sum_{y=-b}^{b} M(x_i + x, y_i + y) \ , \tag{2.1}$$

$$\sigma_M(x_i, y_i) = \sqrt{\frac{1}{n_x n_y} \sum_{x=-a}^{a} \sum_{y=-b}^{b} (M(x_i + x, y_i + y) - \mu_M(x_i, y_i))^2} \ , \tag{2.2}$$

where the size of the neighborhood is $n_x \times n_y$ with $n_x = 2a+1$ and $n_y = 2b+1$. Modeling the reverberation as a Weibull distribution and the target echo as a deterministic value higher than the reverberation mean, a neighborhood containing a target will be separated from neighborhoods containing reverberation in the mean-standard deviation plane, which is illustrated in Figure 2.5. A neighborhood containing only target will have higher mean than a neighborhood containing only reverberation and a standard deviation of zero. A neighborhood containing only reverberation will have a nonzero standard deviation. Neighborhoods containing both target and reverberation will have a mean ranging from the reverberation mean to the target mean depending on the ratio of target and reverberation pixels. The standard deviation will be high if about half of the pixels belong to a target and half of the pixels belong to the reverberation. The standard deviation will be low if the majority of the pixels belong to either a target or the reverberation. Thus the standard deviation will vary from low to high and then back to low as the target pixel ratio is increased. The target is identified as pixels with a neighborhood with either a mean above a threshold or a standard deviation above another threshold. Practically the target echo will not be constant but the variation will be low.

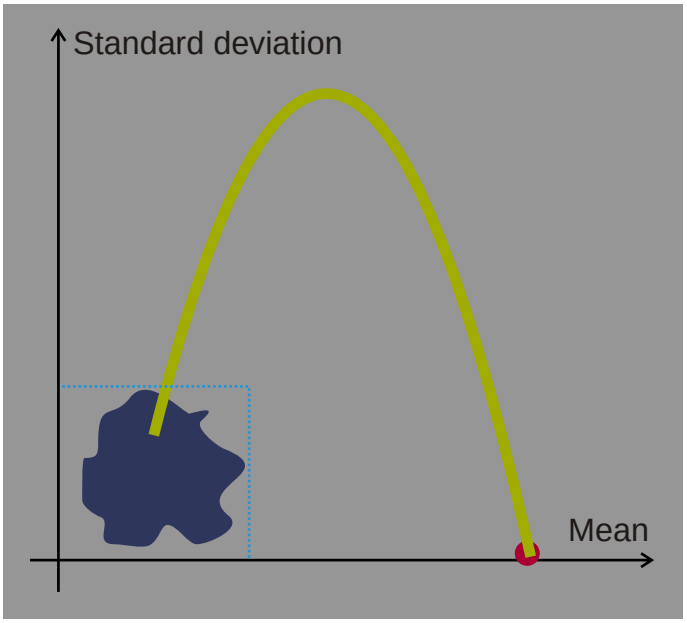

Figure 2.5: Schematic representation of a SAS image in the mean-standard deviation plane. Reverberation is modeled as a Weibull distribution, target echo is modeled as a deterministic value higher than the reverberation mean. Mean and standard deviation is computed in a neighborhood of each pixel. Neighborhoods containing only reverberation are indicated by blue. Neighborhoods containing only target are indicated by red. Finally neighborhoods containing both reverberation and target are indicated by green. Detection thresholds are shown in light blue.

Furthermore the neighborhood size should be selected depending on target size.

2.3.2 Dual Frequency Processing

Denote a $N_x \times N_y$ boolean image D_s originating from sonar, where a pixel value of TRUE or FALSE indicate that a target has been detected at that pixel or not respectively. Now consider two such images originating from a low frequency sonar, D_{LF} and a high frequency sonar, D_{HF}. A similar image containing proud objects is then determined as,

$$D_{proud} = D_{LF} \cap D_{HF} \ , \tag{2.3}$$

where $\cap$ denotes the boolean AND operator performed at each pixel. The buried object are identified as,

$$D_{buried} = D_{LF} \cap \neg D_{HF} \ , \tag{2.4}$$

where $\neg$ denotes the boolean NOT operator. When using images with different resolution the morphological image operations erode and dilate can be used to transform detected targets to equal size.

3 Results

3.1 Simulation

In this section results from the wave propagation modeling and the SAS simulations will be presented. The water column and the bottom parameters used in the models are shown in Table 3.1. Moreover, the parameters of the Weibull

Table 3.1: Water column and bottom parameter values used in the models. See Appendices A and B for details regarding environment parameters.

Parameter	Value
c_1	1430 m/s
ρ_1	1000 kg/m^3
β_1	0 dB/$wavelength$
c_2	1384 m/s
ρ_2	1148 kg/m^3
β_2	0.03 dB/$wavelength$

law in equation (A.17), is set to $\gamma = 4$ and $\zeta = 1.65$ when applicable in the ray trace case. The environment parameters have been obtained from inversion studies and core sample analyses, see Appendix B.

SAS simulations (S.1) were carried out for three different generic targets. The targets were: A sphere with radius 0.25 m, a quadratic box with sides 0.5 m and a cylinder with lenght 1.89 m and radius 0.325 m. In particular the cylinder models the target composed of car tires mounted on an axle, i.e. LCO. In Figure 3.1, resulting SAS images are found for the sphere, the box and the cylinder without bottom scatterers, as well as the cylinder with bottom scatterers. The objects appears as expected and the image of the buried cylinder resembles the image of the buried tires, cf. Figure 3.9.

SAS simulations were carried out for an acoustically rigid cylinder (S.2) using the full-field model. Again a cylinder models the target composed of car tires mounted on an axle. In Figure 3.2, the resulting SAS image is found for the cylinder and should be compared to SASRAY image in Figure 3.1 and field experiment image in Figure 3.9.

As previously mentioned, the dual frequency sonar is supposed to work in two frequency modes in order to discriminate between proud and buried targets. The SAS images in Figure 3.1 were produced with a low frequency sonar. To exemplify the discrimination between proud and buried targets, two point scatterers were utilized (S.3) keeping the remaining SASRAY parameter settings. One scatterer was positioned in the water halfspace 0.5 m above the bottom surface and one scatterer was positioned in the bottom halfspace 0.5 m below the bottom surface. The resulting SAS images for the low and the high frequency mode are found in Figure 3.3. As can be seen in Figure 3.3, the response of the buried scatterer is weaker than the proud one and the difference is more prominent in the high frequency mode. In the low frequency mode the difference in amplitude can be estimated to 1 dB, while the difference in the high frequency mode can be estimated to 4 dB.

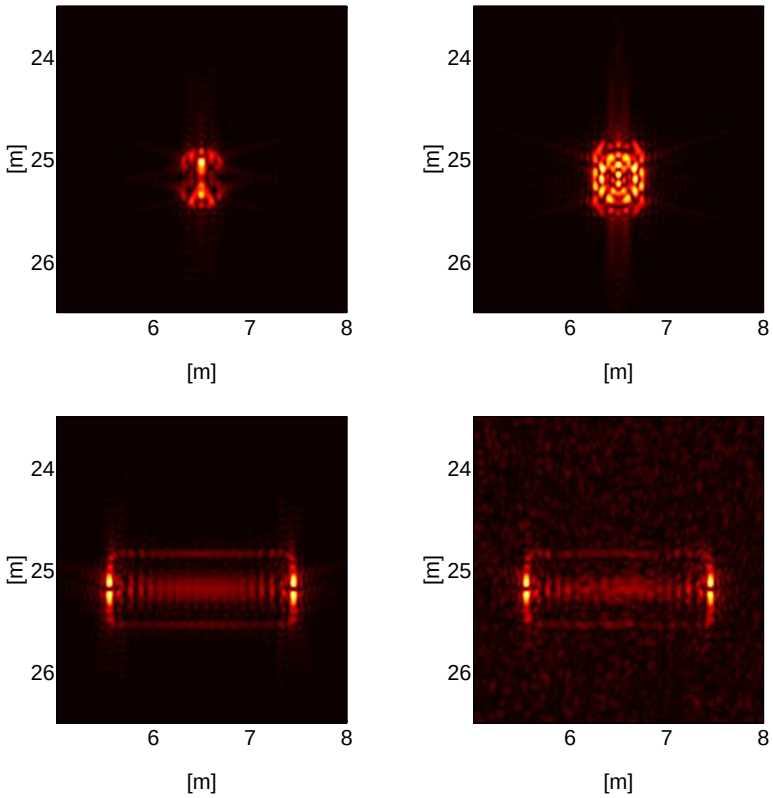

Figure 3.1: SAS images based on 33 pings using the SASRAY model. Sphere (top left), Box (top right), Cylinder (bottom left) and Cylinder with bottom scatterers (bottom right).

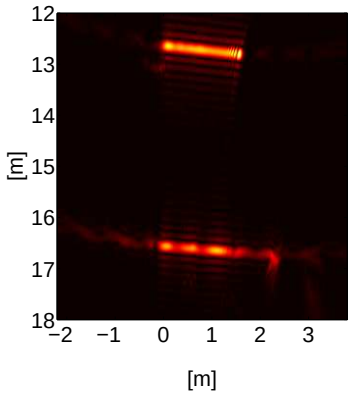

Figure 3.2: SAS image for a cylinder based on 24 pings using full-field modeling.

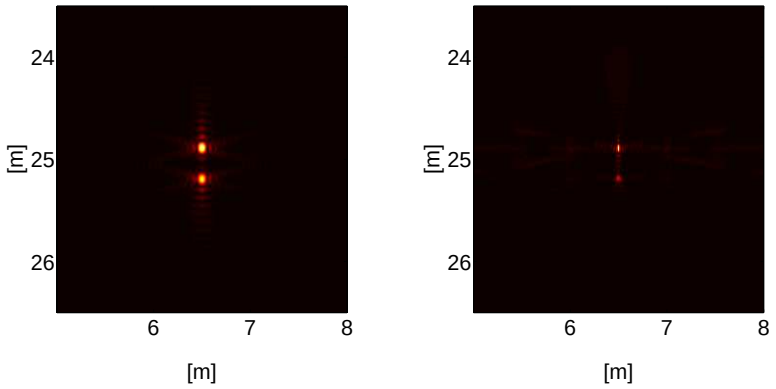

Figure 3.3: Resulting SAS images from the SASRAY model with two point scatterers based on SAS processing of 33 pings. Low frequency mode (left) and high frequency mode (right).

3.2 Field Experiment

To verify that the low frequency SAS equipment transmits and receives the desired signal the first test experiment (T.1) was conducted. An image of the transmitted pulse is shown in figure 3.4 together with a SASRAY simulation of the same setup. The main structure including beamwidth was similar, some discrepancy in sidelobes was however visible.

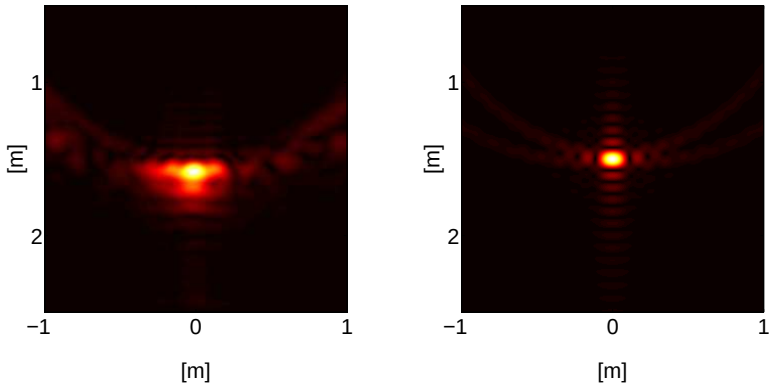

Figure 3.4: A 20 ms 20-30 kHz LFM pulse is emitted by the transmitter and received by the low frequency receiver. Left: measurement, Right: simulation.

A corner reflector was imaged to verify that the transmitter and receiver are properly mounted as a SLS (T.2). The result is shown in Figure 3.5 together with the simulation. Again images showed great resemblance with some minor interference in the measurement.

The third test experiment (T.3) was executed at the test site to verify that low frequency equipment was properly mounted on the carriage. Figure 3.6 show the physical aperture image of a corner reflector from both experimental and simulated data. The result was almost identical. Notice that when comparing to Figure 3.5 the range to the corner reflector is larger and hence resolution decreased.

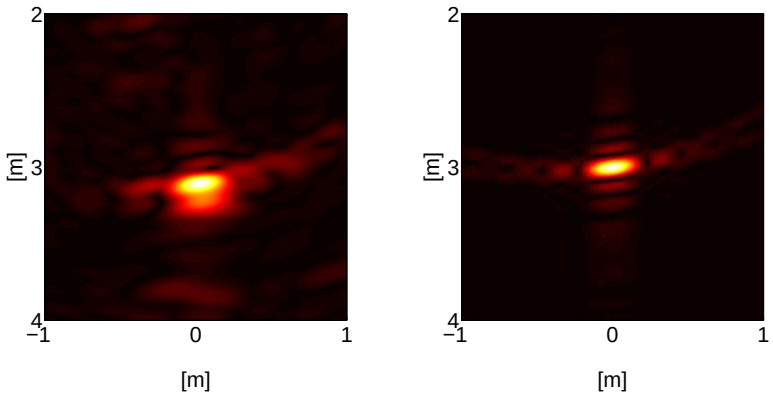

Figure 3.5: Tank laboratory low frequency physical aperture measurement of a corner reflector. Left: measurement, Right: simulation.

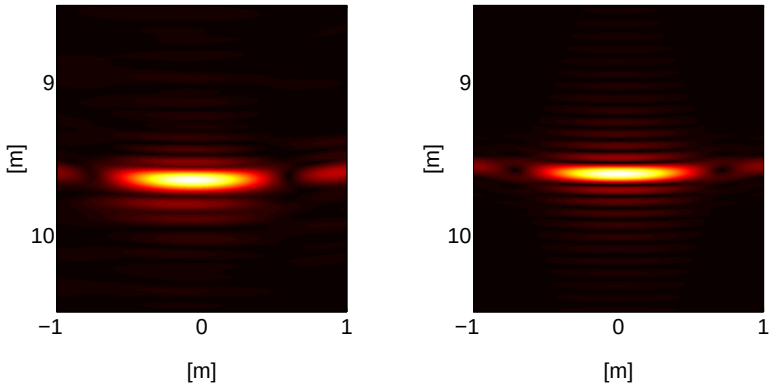

Figure 3.6: Test site low frequency physical aperture measurement of a corner reflector. Left: measurement, Right: simulation.

The last test experiment (T.4) intended for verification of the SAS processing was conducted using the full rail length. The target was again the corner reflector. Field experiment and simulation result are shown in Figure 3.7. Both

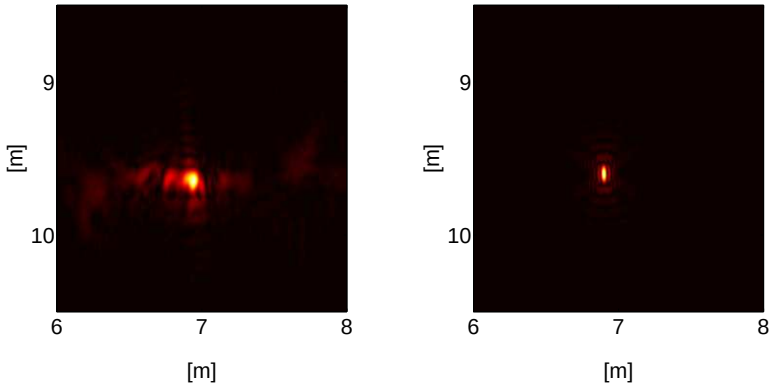

Figure 3.7: SAS image of a corner reflector. Left: measurement, Right: simulation.

images show the same resolution improvement comparing to the physical aperture images in Figure 3.6, however some sidelobe smearing is present in the experimental data. Although the corner reflector appears as a point reflector for each individual ping, the reflection point will move as the corner reflector is view from different angles resulting in the characteristic sidelobe pattern. In

the simulation the corner reflector was approximated by a point reflector giving a perfect sidelode pattern.

Four measurements were carried out with the dual frequency sonar. Two of the runs were intended for detection of the buried objects (F.1-F.2) and the other two (F.3-F.4) for the detection of objects placed on the sea bottom. The buried objects were a car tire target LCO, and two mine like objects, the small one and the large one, SMLO and LMLO, respectively. Resulting SAS images of the experimental area for the buried objects are shown in Figure 3.8. In the left

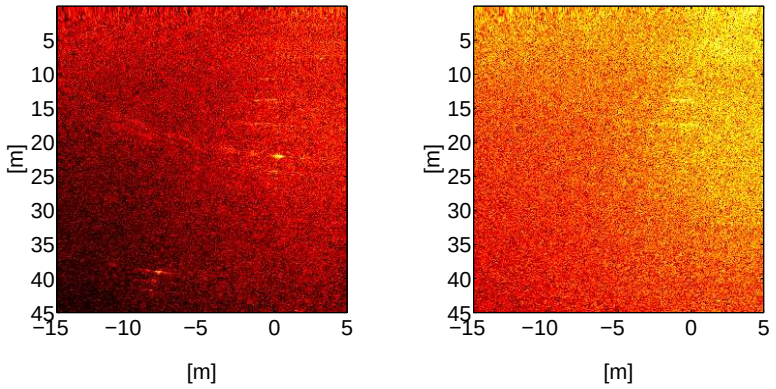

Figure 3.8: Left frame: SAS image of target area with corner reflectors at the coordinates (0,22) for the SMLO and (-8,39) for the LMLO. Right frame: SAS image of target area without corner reflectors.

frame originating from setup (F.1), three objects are visible, the LCO and two corner reflectors. The LCO is located at the x-coordinate 0 and y-coordinate 10. From now on this position will be denoted by (0,10). The corner reflectors are located at (0, 22) and (-8,39) and are placed on the top of the SMLO and the LMLO in order to mark their positions. As can be seen from the left frame all three objects are more or less detected as a triple image of each object. Images of the LCO are also visible at (0,14) and (0,18). This triple imaging can be explained as reflections in a calm sea surface. The sonar is transmitting and receiving energy with a broad vertical beam width incorporating the water surface and therefore making multiple path ways possible. In the right frame of Figure 3.8, the two corner reflectors are removed (F.2). Only the LCO remains as a detected object, also here as a triple image. Any trace of the two mine like objects is not seen in this imaging. Enlarged SAS images of the buried objects are shown in Figure 3.9. The LCO is detected as a 1.3 m long and 0.1-0.2 m

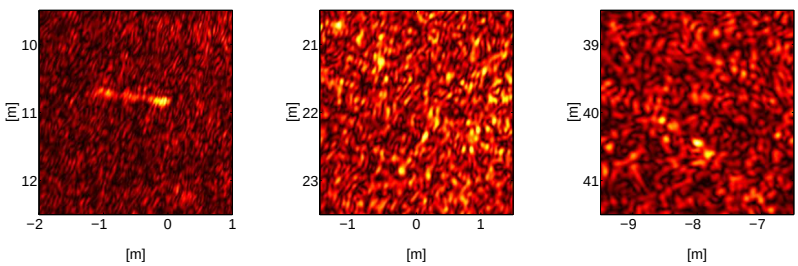

Figure 3.9: SAS images of the three buried objects shown in enlarged parts of the right frame of Figure 3.8. From left the LCO, the SMLO and the LMLO.

wide object. The SMLO is not resolved in back scattered signal from the sea bottom. The same detection result appears to arise for the LMLO. Even if there is a line of bright spots in the right frame in Figure 3.9, it is uncertain whether it can be regarded as detection or not of one of the edges of the LMLO. When preparing the target area the divers were instructed to bury the LMLO with its length axis in an oblique angle to the longitudinal extension of the area; a fact, however, that could speak in favor for detection of a buried target.

The target area for buried objects is unfortunately not reachable for the high frequency sidescan sonar, as being mounted on the same carriage as the SAS. Images from the low frequency SAS and high frequency sidescan sonar can therefore not be compared and a verification of the difference in bottom penetrating properties of low frequency and high frequency sonar cannot be made using the MLOs.

The six bottom laid targets used in this field experiment (F.3-F.4) are a EPS cement sphere, a EPS cement brick, a EPS cement truncated cone, an aluminum ladder, an aluminum plate on a stand and a stone of granite attached to a steel bar with a steel plate.

In order to compare the performance of the two sonar a number of targets were placed on the sea bottom in front of the rail and within the visible area of both the high frequency sidescan sonar and the low frequency SAS. In a first run (F.2) the experimental area is examined without any placed objects. The SAS images are seen in Figure 3.10. From the sidescan image two objects

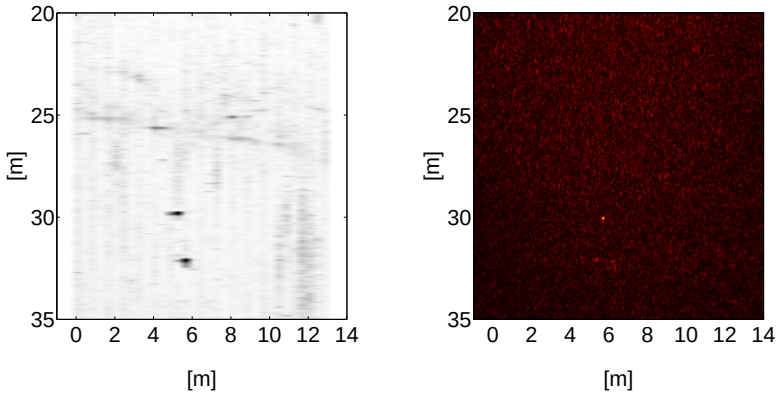

Figure 3.10: A sidescan image (left) and a SAS image (right) of the empty experimental area for proud targets.

are clearly detected, at about (5,30) and (6,32), respectively. There are also some additional objects seen in the sidescan image with less contrast to the background, like an elongated object in the upper right corner which might be a cable and some smaller object in the middle of the image. In the SAS image only one of the objects is clearly detected, the object at (5, 30). The object at (6, 32) is seen only as a faint spot. Just to the left of the faint spot, a sea surface reflection of the first object is seen, cf. the corner reflectors in Figure 3.8. The presumed cable and the other object in the middle of the target area are not seen in the SAS image.

With the brick, the truncated cone and the sphere placed on the sea bottom, (F.3) the sonar images will show up as in Figure 3.11. The coordinates for the objects are (10, 22), (12, 28), and (6, 29), respectively. Ropes tied to each object are seen as light streaks extending to the right in the images. Objects seen in the side scan image is also seen in the SAS image and vice versa, with

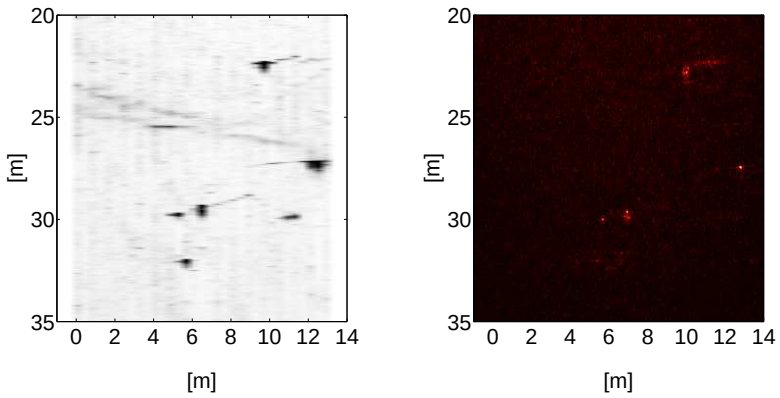

Figure 3.11: A sidescan image (left) and a SAS image (right) of the experimental area for proud targets with the brick (10,22), the truncated cone (12,27) and the sphere (6,30).

one exception. An extra, unknown object is visible in the sidescan image at (11, 30). Figure 3.12 shows three enlarged SAS images. Looking at the images

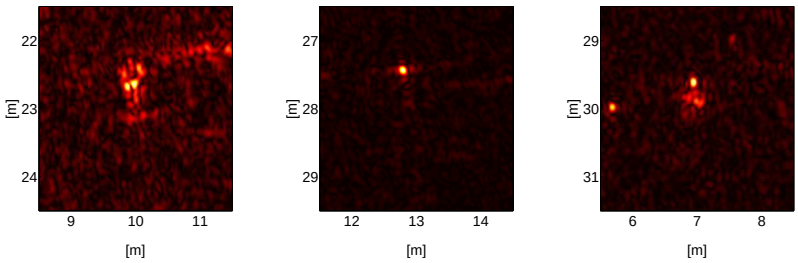

Figure 3.12: SAS images of the brick, the truncated cone, and the sphere.

from right to left, the sphere and the cone are imaged as point targets. The bright area below the spot might be the lead weight attached to the sphere in the rightmost image of Figure 3.11. Note also the bright spot at (5.5,30). This is the earlier detected object in the empty experimental area, in that image indicated at (5,30). The brick or the boxlike object seems to have a certain extension. The rope extending rightward is also visible and perhaps also the lead weights right below the brick.

Exchanging objects (F.4), the scenery turned into what is shown in Figure 3.13. The stone, the ladder, and the plate on the stand were the new objects placed on the sea bottom. The ladder is furthermore provided with weights. All three objects are easily identified in both images of Figure 3.13. The ladder is identified as the horizontally elongated object at (6-10,28). Above the ladder is the stone located at (8,24) and below the ladder to the right, the plate is imagined at (11,32). Ropes extending from the objects are detected as in the experiment before. In the SAS image all three objects are imaged in duplicate due to the reflections in the water surface and the plate on the stand is imaged as a more extended object than the stone.

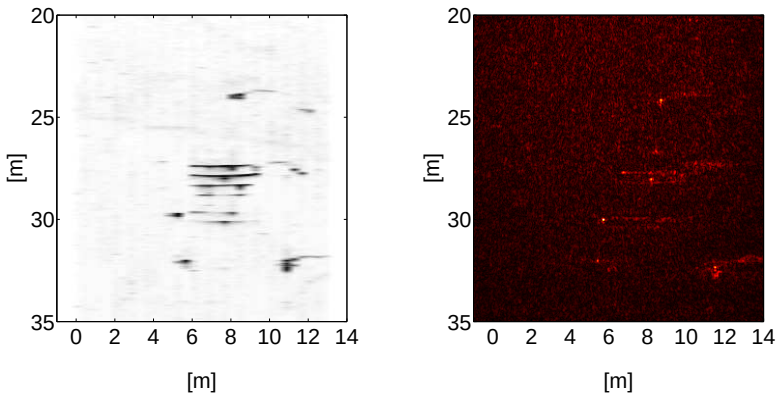

Figure 3.13: A sidescan image (left) and a SAS image (right) of the experimental area for proud targets with the stone (8,24), the ladder (6-10,28) and the plate (11,32).

A closer look at image of the ladder in Figure 3.14 shows a double horizontal streak from about 6.5 m on the x-axis to about 9.5 m. The bright spot in the

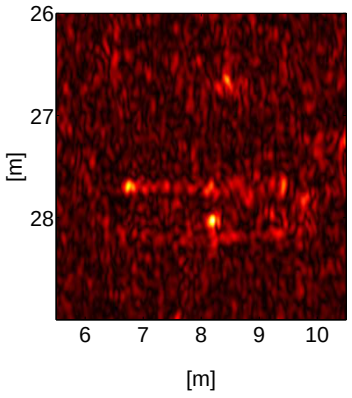

Figure 3.14: SAS image of the ladder.

middle of the ladder are some attached extra weights. The bright area at (8.5,26.5) is the stone mirrored in the water surface. The SAS images of the stone and the plate are found in Figure 3.15. In both images the ropes are visible. The stone is imaged more or less as a point target even if it has some extension. The plate or the stand has one bright spot and an extended bright area below possibly indicating a complex target of at least a certain size.

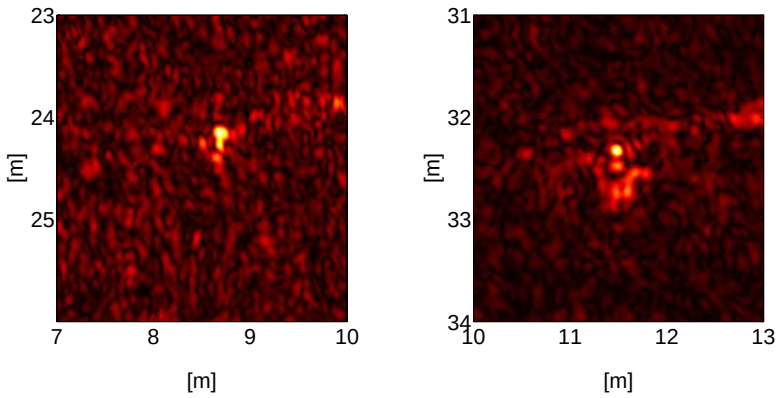

Figure 3.15: SAS image of the stone (left) and the plate with the stand (right).

3.3 Signal Processing

To evaluate the proposed detection algorithm one of the SAS images in figure 3.12 was used. The image originated from field experiment setup (F.3) using the low-frequency SAS and contained an image of the truncated cone. The result is shown in figure 3.16. Since the image contained a simple object with one bright scatter point the algorithm easily segmented the target from the reverberation background.

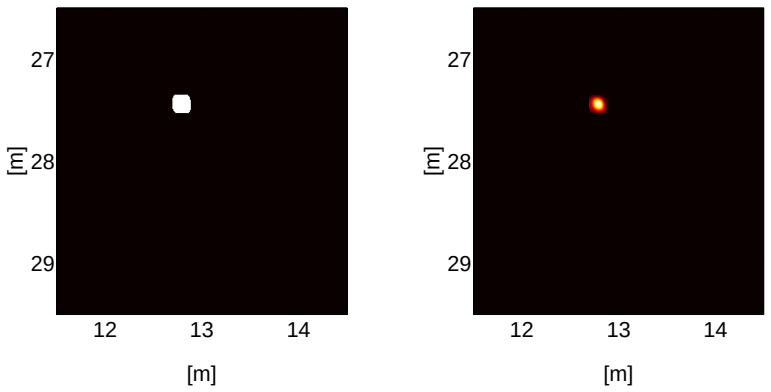

Figure 3.16: Detection of the truncated cone from Figure 3.12. The left panel shows the boolean detection image and the right panel shows the segmented SAS image.

A larger scene containing several targets and varying reverberation is a more difficult task. The detection algorithm was therefore given the two low-frequency SAS full scene images from experimental setups (F.3) and (F.4). Figures 3.17 and 3.18 shows the result from (F.3) and (F.4) respectively. From setup (F.3) the proud targets were detected and segmented together with the surface reflected buried tires. In figure 3.18 the proud objects were partly detected together with the surface reflection and parts of the direct path of the buried tires.

The separation of buried objects from bottom objects were tested on simulated SAS images from setup (S.4). A high- and low frequency SAS of the cylinders, one buried and one proud, were generated. The high frequency SAS image is shown in figure 3.19 together with the segmented target after running

the detection algorithm. As expected only the proud cylinder is visible and almost perfectly segmented. Similar images from the low frequency SAS is shown in figure 3.20. Here both targets are visible and well segmented. Notice that the decreased resolution produced a different appearance. After dual frequency processing the result in figure 3.21 was achieved.

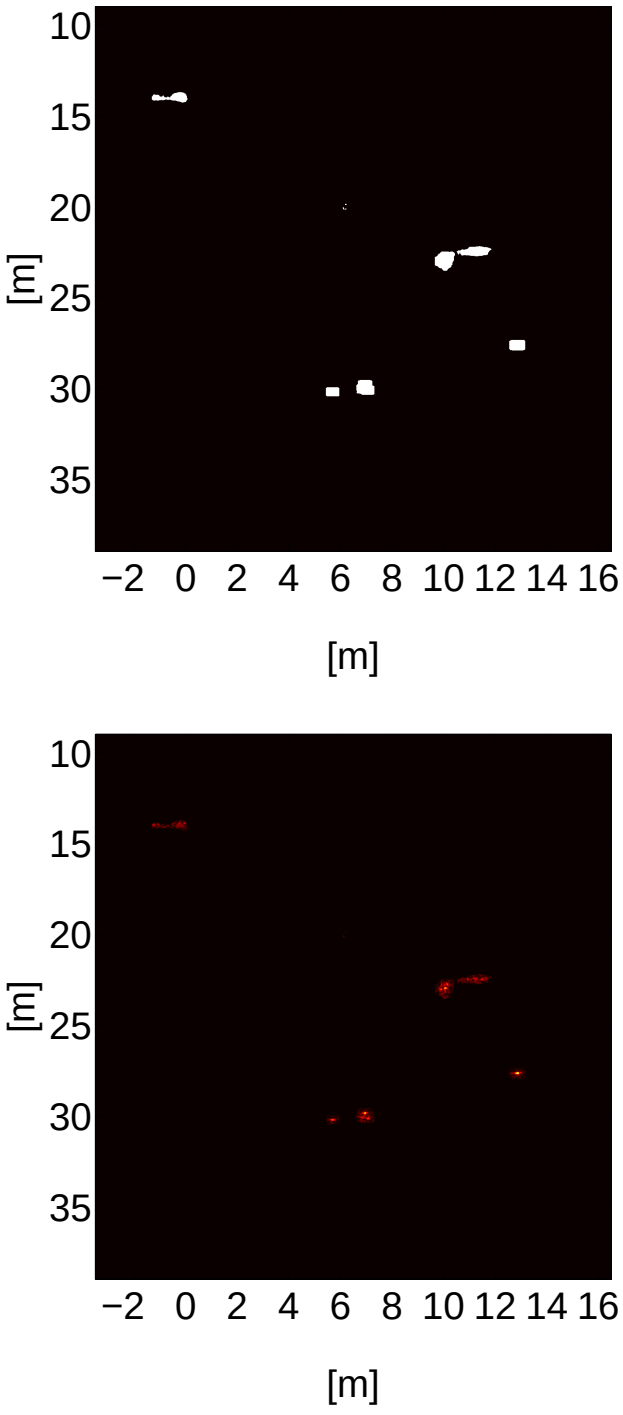

Figure 3.17: Detection of the tragets from experimental setup (F.3). The top panel shows the boolean detection image and the bottom panel shows the segmented SAS image.

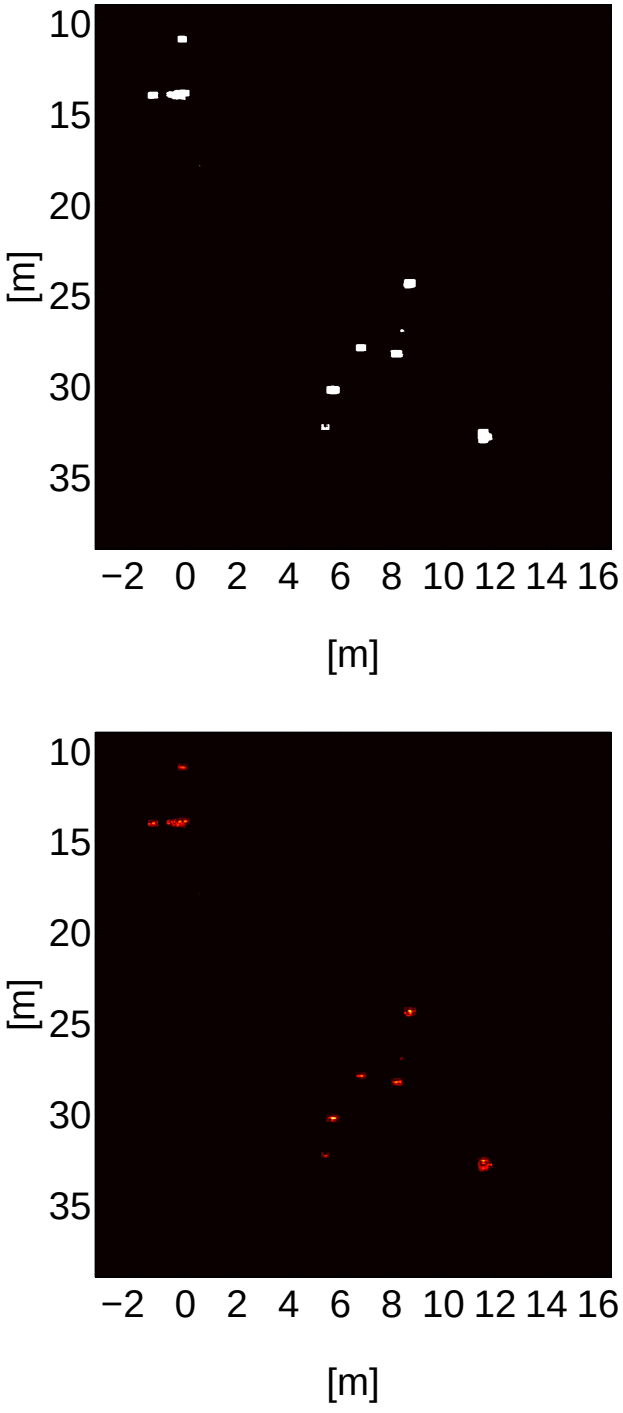

Figure 3.18: Detection of the targets from experimental setup (F.4). The top panel shows the boolean detection image and the bottom panel shows the segmented SAS image.

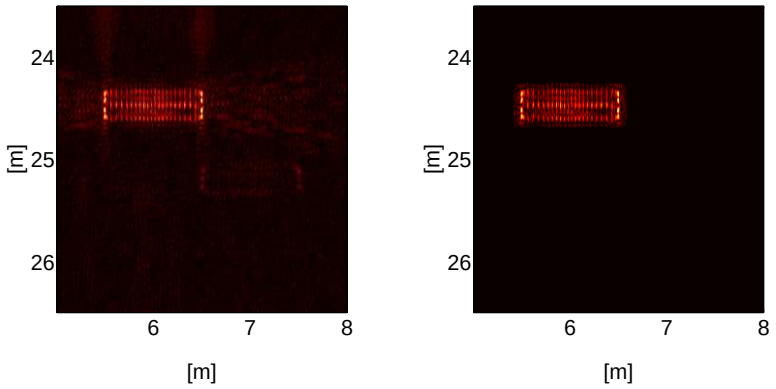

Figure 3.19: Detection of the targets from simulation setup (S.4) using the high frequency SAS. The left panel shows the original SAS image and the right panel shows the segmented SAS image.

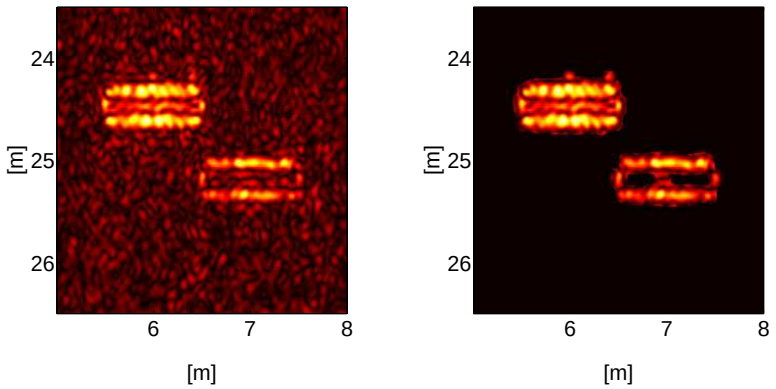

Figure 3.20: Detection of the targets from simulation setup (S.4) using the low frequency SAS. The left panel shows the original SAS image and the right panel shows the segmented SAS image.

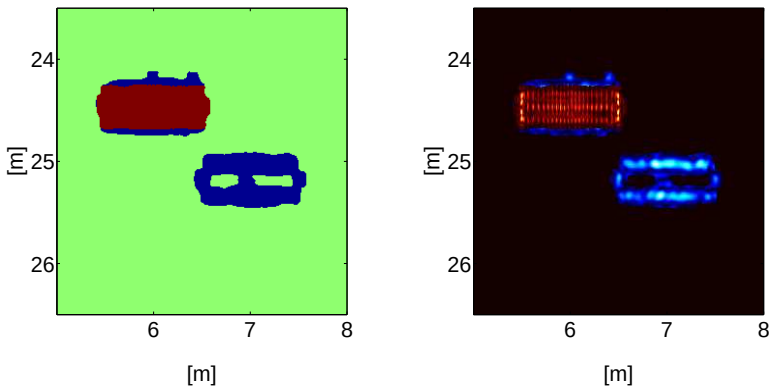

Figure 3.21: Detection of the targets from simulation setup (S.4) using the dual frequency SAS. The left panel shows the detection image where red indicate proud object and blue buried object. The same result is shown in the right panel were the original image has been segmented and presented using different color coding for proud and buried objects.

4 Discussion

With the ambition to improve future MCM operations the dual frequency sonar was studied. The dual frequency possibilities were studied using simulations and field experiments. The work included: the development of a fast ray tracing model, the deployment and testing of a new receiver array for low frequency SAS, the deployment of a sidescan sonar for high frequency imaging and the implementation of signal processing code for detection and separation of proud and buried objects.

The simulations were intended to study the ability to detect and discriminate proud and buried objects with a combination of low and high frequency SAS. Furthermore the simulations supported the design of the field experiment. The first simulation (S.1) showed that target shapes in SAS images were recognizable and similar to images from field data. A comparison with the full-field model (S.2) verified that major parts of the structures were captured by the ray tracing, why it was concluded that the ray tracing model was applicable for the rest of the study. The third simulation (S.3) showed a reduction of the reflected energy from buried targets when the center frequency was increased.

The receiver array for low frequency SAS and the sidescan sonar for high frequency imaging were deployed at the rail based SAS facility in Djupviken. The objective of the field experiment was to investigate if buried and proud objects can be discriminated by a combination of low and high frequency sonar. In the two first experimental setups (F.1,F.2) one of the buried objects was identified in the low frequency mode. However, it turned out that this object was not insonified in the high frequency mode. Additional SAS images of proud objects in setups (F.3,F.4) were generated and identified using both the low frequency SAS and the high frequency sidescan sonar.

A first version of signal processing code for detection and discrimination of proud and buried objects has been implemented. The code was used on both simulated and measured data. The purpose was to evaluate a detection method described in the literature and extend it to discriminate buried and proud objects. Low frequency SAS images from experiments (F.3) and (F.4) were fed to the algorithm and the proud objects were segmented. Using images from simulation (S.4), buried objects were discriminated from proud objects using dual frequency processing.

It is recommended that the ray tracing model SASRAY is extended to handle layered media, as well as a more detailed treatment of the reflection losses and the ability to model source directivity. This will improve the modeling of penetration into the seabed. In addition, experimental studies of penetration into the seabed should be conducted. It would be valuable to test the dual frequency sonar in another environment (e.g. with a sand bottom). The signal processing algorithm is promising but more data, simulated and measured, are needed to draw further conclusions. Several detection algorithms are described in the literature, and their performance should also be considered.

References

[1] Nationalencyklopedin. Sjöfart. http://www.ne.se/artikel/306690, 2008-12-04.

[2] B. Lövgren. CAD/CAC and autopositioning enhances AUV minehunting efficiency. In *Proceedings of UDT Europe*. Napoli, Italy, 2007.

[3] R.E. Hansen, H.J. Callow, T.O. Sæbø, P.E. Hagen and B. Langli. High fidelity synthetic aperture sonar products for target analysis. In *Proceedings of OCEANS 08*. Quebec City, Canada, 2008.

[4] R.H. Wilkens and M.D. Richardson. Guest Editorial. Special issue on mine burial process. *IEEE Journal of Oceanic Engineering*, 32(1):1–2, 2007.

[5] R.H. Wilkens and M.D. Richardson. Mine burial prediction: A short history and introduction. *IEEE Journal of Oceanic Engineering*, 32(1):3–9, 2007.

[6] P. Morén and J. Pihl. Sub-bottom characterization using a parametric sonar. In *Proceedings of Oceans 98*, pages 1828–1832. IEEE/OES, Nice, France, 1998.

[7] S. Ivansson, I. Karasalo, P. Morén, J. Pihl and P. Söderberg. Acoustical methods for detection of buried objects. Technical Report FOA-R–00-01616-409–SE, Swedish Defence Research Establishment, 2000.

[8] P. Morén, N. Jacobsen and P. Söderberg. Metoder för undersökning av objekt i bottensediment - fältförsök i Möja Söderfjärd. Technical Report FOI Memo Dnr 03-1444:2, Swedish Defence Research Agency, 2003, In Swedish.

[9] I. Karasalo and P. Skogqvist. Inverse bistatic acoustic scattering for identification of buried objects. Technical Report FOI-R–1343–SE, Swedish Defence Research Agency, 2004.

[10] M.A. Pinto, A. Bellettini, R. Hollett and A. Tesei. Real- and synthetic-array signal processing of buried targets. *IEEE Journal of Oceanic Engineering*, 27(3):484–494, 2002.

[11] J.E. Piper, K.W. Commander, E.I. Thorsos and K.L. Williams. Detection of buried targets using a synthetic aperture sonar. *IEEE Journal of Oceanic Engineering*, 27(3):495–504, 2002.

[12] S. Dugelay, S.A. Chapman and R. Orme. Parametric Synthetic Aperture Sonar for the Detection of Buried Mines: A Feasibility Study. In *Synthetic Aperture Sonar and Synthetic Aperture Radar*. Underwater Acoustics Group of the Institute of Acoustics in association with the Aerospace and Electronic Systems Society of the IEEE, Lerici, Italy, 2006.

[13] A. Belkacem, K. Besbes, J. Châtillon and M.E. Zakharia. Planar SAS for Sea Bottom and Subbottom Imaging: Concept Validation in Tank. *IEEE Journal of Oceanic Engineering*, 31:614–627, 2006.

[14] L.J. Cutrona. Comparison of sonar system performance achievable using synthetic-aperture techniques with the performance achievable by more conventional means. *Journal of the Acoustical Society of America*, 58(2):336–348, 1975.

[15] M. Jönsson and Ö. Staaf. Lägesrapport: Utveckling av experimentell utrustning för aktiv syntetisk apertur sonar. Technical Report 03-2233, Swedish Defence Research Agency, 2003, In Swedish.

[16] M. Jönsson. Lägesrapport: Fältförsök med ny utrustning för syntetisk apertur sonar. Technical Report FOI Memo 1005, Swedish Defence Research Agency, 2004, In Swedish.

[17] M. Jönsson, J. Pihl and M. Åklint. Imaging of buried objects by low frequency SAS. In *Proceedings of Oceans 2005*. MTS/IEEE, Brest, France, 2005.

[18] S. Ivansson, N. Jacobsen, M. Levonen, B. Nilsson, P. Morén and P. Söderberg. Akustisk detektion av begravda objekt. Technical Report FOI-R–0324–SE, Swedish Defence Research Agency, 2000, In Swedish.

[19] Ö. Staaf, N. Jacobsen, M. Jönsson, P. Morén, J.Pihl and M. Åklint. Undersökning av bottenpenetration vid snett infall. Technical Report FOI Memo 1815, Swedish Defence Research Agency, 2006, In Swedish.

[20] M. Zakharia, Y. Chevriaux, G. Doignon, J. Dybedal, R. Legallo and C. Pollet. SITAR prototype, a parametric synthetic sidescan sonar. In *Proceedings of Seventh European Conference on Underwater Acoustics*. TNO, Delft, The Netherlands, 2004.

[21] P.T. Gough, M.A. Noonchester, A.J. Hunter and M.P. Hayes. Imagery from a Multi-Frequency SAS: A Comparison of Simulated and Experimental Results. In *Synthetic Aperture Sonar and Synthetic Aperture Radar*. Underwater Acoustics Group of the Institute of Acoustics in association with the Aerospace and Electronic Systems Society of the IEEE, Lerici, Italy, 2006.

[22] J.E. Piper and R. Lim. Small Object Detection with a Dual-Frequency Synthetic Aperture Sonar. In *Synthetic Aperture Sonar and Synthetic Aperture Radar*. Underwater Acoustics Group of the Institute of Acoustics in association with the Aerospace and Electronic Systems Society of the IEEE, Lerici, Italy, 2006.

[23] F. Maussang, J. Chanussot, A. Hétet and M. Amate. Mean-standard deviation representation of sonar images for echo detection: Application to SAS images. *IEEE Journal of Oceanic Engineering*, 32(4):956–970, 2007.

[24] S. Reed, Y. Petillot and J. Bell. An automatic approach to the detection and extraction of mine features in sidescan sonar. *IEEE Journal of Oceanic Engineering*, 28(1):90–105, 2003.

[25] M. Montanari, J.R. Edwards and H. Schmidt. Autonomous underwater vehicle-based concurrent detection and classification of buried targets using higher order spectral analysis. *IEEE Journal of Oceanic Engineering*, 31(1):188–199, 2006.

[26] A. Cederholm and M. Jönsson. AUV-based minehunting - A resolution perspective. Technical Report FOI-R–2406–SE, Swedish Defence Research Agency, 2007.

[27] F.B. Jensen, W.A. Kuperman, M.B. Porter and H. Schmidt. *Computational ocean acoustics*. Springer-Verlag, 1994.

[28] I. Karasalo. On evaluation of hypersingular integrals over smooth surfaces. *Computational Mechanics*, 40(3):617–625, 2007.

[29] L. Abrahamsson. RAYLAB - a ray tracing program in underwater acoustics. Technical Report FOI-R–1047–SE, Swedish Defence Research Agency, 2003.

[30] H. Gothäll and R. Westin. Evaluation of four global optimisation techniques (ASSA, DE, NA, Tabu Search) as applied to anechoic coating design and inverse problem uncertainty estimation. Technical Report FOI-R–1593–SE, Swedish Defence Research Agency, 2005.

[31] B. Berntsen, I. Karasalo, M. Levonen, P. Morén and V. Westerlin. Seabed characterisation in the Baltic with the SIROB and FARIM methods. Technical Report FOA-R-99-01237-409-SE, Swedish Defence Research Establishment, 1999.

[32] T. Andrén and G. Lindberg. Analysis of physical and chemical properties of two piston cores. Technical report, Firma Thomas Andrén, 1998.

A Ray Tracing Model

Some notation rules and definitions are required for the description that will follow. Two coordinate systems will be utilized, a Cartesian system (x, y, z) and a spherical system (r, θ, ϕ). Geometrical vectors defined in a Cartesian system are written in bold small letters ($\boldsymbol{r}$) and bold small letters with subindices ($\boldsymbol{r}_{,x}$,$\boldsymbol{r}_{,y}$,$\boldsymbol{r}_{,z}$) denote the corresponding coordinate values. In addition, the sign function will be used frequently denoted by $sgn()$. Regarding environmental parameters of fluid or solid medium, the density and the sound velocity are denoted by ρ and c respectively. For a given frequency f, the wavelength is given by $\lambda = c/f$. Denote by β the attenuation in dB per wavelength. The total attenuation over a distance d then equals $\beta d/\lambda$ dB. Parameters ρ, c, λ and β with subindices indicate that several materials are involved.

The working name of the ray tracing model is SASRAY. Ray tracing models are based on a high frequency approximation which might lead to coarse accuracy in the results at lower frequencies. Low frequencies are here understood to be frequencies with wavelengths of the same order as the spatial scale of the variations in the environmental parameters, such as the sound velocity. However, the great advantage with this technique is its high computational speed: Once the rays are traced the field can be computed for all frequencies of interest with little extra cost.

In Figure A.1, an idealized configuration is sketched, which is the configuration that can be handled presently by SASRAY. Since the media consists of

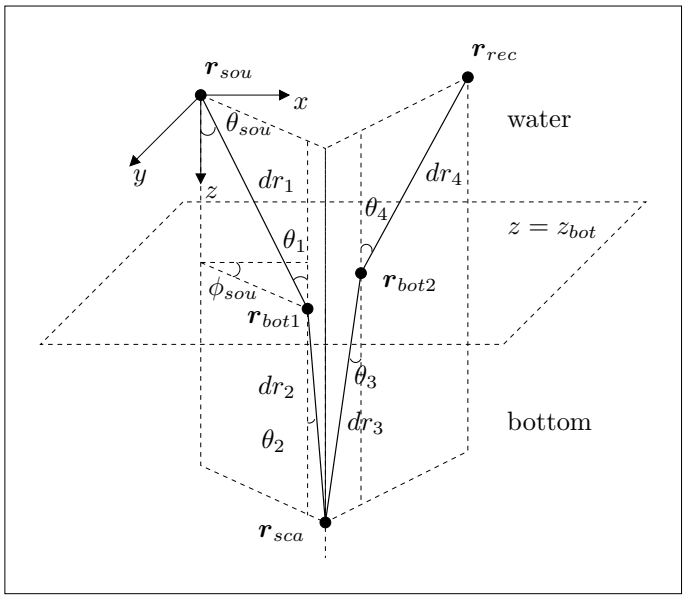

Figure A.1: An example of a configuration including positions of source, scatterer, receiver and halfspaces, which can be handled by SASRAY.

two homogeneous halfspaces (water and bottom), the ray joining the positions of the source ($\boldsymbol{r}_{sou}$), the point scatterer ($\boldsymbol{r}_{sca}$) and the receiver ($\boldsymbol{r}_{rec}$), consists of the straight ray segments (dr_1, dr_2, dr_3, dr_4) within each halfspace. For each configuration of source, point scatterer and receiver two unique intersections can be determined. The ray slope then has discontinuities at the intersections

($\boldsymbol{r}_{bot1}$,$\boldsymbol{r}_{bot2}$) located at the horizontal interface ($z = z_{bot}$), cf. Figure A.1. Furthermore, source angles $(\theta_{sou}, \phi_{sou})$ and intermediate angles θ_1, θ_2, θ_3 and θ_4 are defined in relation to the ray segments. The spherical angles are constrained to $\theta \in [0, \pi]$ and $\phi \in [0, 2\pi]$. The details of handling ray trajectories are found in Section A.1.

The shape and the amplitude of the received signals also depend on different kinds of loss mechanisms along the ray paths: For example, losses due to geometrical spreading, transmission through interfaces between different media and attenuation due to absorption and scattering in the media. These mechanisms are treated in Section A.2.

The directivity and the beam width of the source affect the shape and the amplitude of the received signal. The source strength factor for each ray should be determined from the transmitted beamform expressed in the spherical (θ, ϕ)-angles, cf. $(\theta_{sou}, \phi_{sou})$ in Figure A.1. The computation of the source strength factors is at this stage not implemented and temporarily this factor is set to 1. For more details regarding the source pulse generation see Section A.3.

With the transmitter/receiver configuration, the selection of source pulse and the ray tracing framework, SASRAY utilizes point scatterers to model both targets and reverberation. The received signal at each receiver is the coherent sum of the contributions of the transmitted signals from a set of sources. These signals have propagated along all rays between the sources and the receiver that contain a point scatterer in the ray trajectory. Target- and reverberation models are briefly explained in Section A.4.

A.1 Ray Trajectories

In figure A.2, the configuration of a source ($\boldsymbol{r}_{sou}$) and a point scatterer ($\boldsymbol{r}_{sca}$) is found, in relation to an assumed arbitrary ray path between two homogeneous halfspaces, i.e. water and bottom, with sound velocity c_1 and c_2 respectively. The boundary between the halfspaces is assumed to be oriented at $z = z_{bot}$ and the ray trajectory is found in a plane perpendicular to the plane defined by the x and y axis, cf. Figure A.1. This configuration along with the lengths l_1, l_2, d_1 and d_2 and the angles θ_1 and θ_2 defined in figure A.2, forms the basis for the calculation of the intersections $\boldsymbol{r}_{bot}$ between the rays and the horizontal interface. The refraction of the rays at the horizontal interface is governed by Snell's law of refraction [27]. By using Snell's law and the geometrical relations given in the equations (A.1)-(A.4) that follows,

$$\frac{\cos\theta_1}{c_1} = \frac{\cos\theta_2}{c_2} \ , \tag{A.1}$$

$$l = l_1 + l_2 = \sqrt{(\boldsymbol{r}_{sou,x} - \boldsymbol{r}_{sca,x})^2 + (\boldsymbol{r}_{sou,y} - \boldsymbol{r}_{sca,y})^2} \ , \tag{A.2}$$

$$d_1 = |\boldsymbol{r}_{sou,z} - z_{bot}| \ , \ d_2 = |\boldsymbol{r}_{sca,z} - z_{bot}| \ , \tag{A.3}$$

$$\cos\theta_1 = \frac{l_1}{(l_1^2 + d_1^2)^{1/2}} \ , \ \cos\theta_2 = \frac{l - l_1}{((l - l_1)^2 + d_2^2)^{1/2}} \ , \tag{A.4}$$

a fourth order polynomial in one of the length parameters can be derived. If the polynomial is written in l_1, the root which is real valued and $l_1 \in [0, l]$ is kept and the corresponding intersection is calculated as,

$$\boldsymbol{r}_{bot} = \left[\boldsymbol{r}_{sou,x} + \frac{sgn(\Delta x) l_1 |\Delta x|}{(\Delta x^2 + \Delta y^2)^2}, \boldsymbol{r}_{sou,y} + \frac{sgn(\Delta y) l_1 |\Delta y|}{(\Delta x^2 + \Delta y^2)^2}, z_{bot}\right] \ , \tag{A.5}$$

using

$$\Delta x = \boldsymbol{r}_{sca,x} - \boldsymbol{r}_{sou,x} \quad , \quad \Delta y = \boldsymbol{r}_{sca,y} - \boldsymbol{r}_{sou,y} \ . \tag{A.6}$$

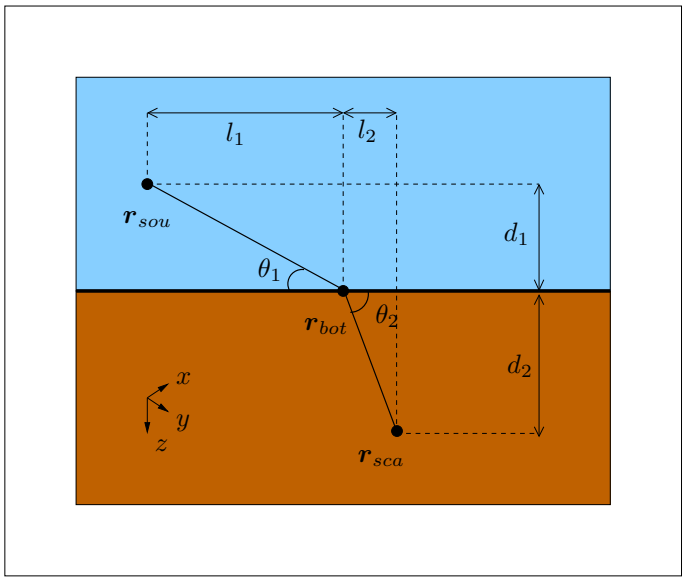

Figure A.2: Configuration of source and point scatterer in relation to corresponding ray path and its intersection between two homogeneous halfspaces, i.e. water and bottom.

The (x, y, z)-coordinates of the ray trajectory points are required and the handling of point scatterers in water halfspaces and bottom halfspaces are treated separately. If a point scatterer lies in the water halfspace, or on the horizontal plane separating the halfspaces, the ray path between the source and the receiver consists of three trajectory points $(\boldsymbol{r}_{sou}, \boldsymbol{r}_{sca}, \boldsymbol{r}_{rec})$, i.e. two straight line ray segments. The spherical launch angles $(\theta_{sou}, \phi_{sou})$ of the rays joining the source and the point scatterer are given by

$$\theta_{sou} = arccos\left(\frac{\boldsymbol{r}_{sca,z} - \boldsymbol{r}_{sou,z}}{|\boldsymbol{r}_{sca} - \boldsymbol{r}_{sou}|}\right) , \tag{A.7}$$

$$\phi_{sou} = arctan\left(\frac{\boldsymbol{r}_{sca,y} - \boldsymbol{r}_{sou,y}}{\boldsymbol{r}_{sca,x} - \boldsymbol{r}_{sou,x}}\right) . \tag{A.8}$$

If a point scatterer lies in the bottom halfspace, as in Figure A.1, the ray trajectory consists of four segments. For each configuration of source, point scatterer and receiver $(\boldsymbol{r}_{sou}, \boldsymbol{r}_{sca}, \boldsymbol{r}_{rec})$ two intersections $\boldsymbol{r}_{bot1}$ and $\boldsymbol{r}_{bot2}$ are uniquely determined in the plane $z = z_{bot}$. Hence, the ray path between the source and the receiver consists of five trajectory points $(\boldsymbol{r}_{sou}, \boldsymbol{r}_{bot1}, \boldsymbol{r}_{sca}, \boldsymbol{r}_{bot2}, \boldsymbol{r}_{rec})$, i.e. four straight line ray segments. The spherical launch angles $(\theta_{sou}, \phi_{sou})$ of the ray joining the source and the point scatterer are given by

$$\theta_{sou} = arccos\left(\frac{\boldsymbol{r}_{bot1,z} - \boldsymbol{r}_{sou,z}}{|\boldsymbol{r}_{bot1} - \boldsymbol{r}_{sou}|}\right) , \tag{A.9}$$

$$\phi_{sou} = arctan\left(\frac{\boldsymbol{r}_{bot1,y} - \boldsymbol{r}_{sou,y}}{\boldsymbol{r}_{bot1,x} - \boldsymbol{r}_{sou,x}}\right) . \tag{A.10}$$

The travel times along the rays are computed as follows. If a point scatterer lies in the water halfspace, the travel time along the rays is given by $T_{travel} = (dr_1 + dr_2)/c_1$. If a point scatterer lies in the bottom halfspace, ray segments 1 and 4 lie in the water, and segments 2 and 3 lie in the bottom. In this case the travel time along the rays is given by $T_{travel} = (dr_1 + dr_4)/c_1 + (dr_2 + dr_3)/c_2$.

A.2 Ray Loss Mechanisms

The total loss factor along the rays is the product of several factors and these can be categorized as follows:

- geometrical spreading loss,
- media attenuation loss,
- losses due to transmission through layer interfaces,
- reflection loss at scatterers,
- losses due to shadowing effects,
- phase shifts due to surface reflections.

Since the halfspaces are homogeneous, it follows that the geometrical spreading loss is spherical. Thus the geometrical loss factor along the rays is proportional to the inverse of the length of the rays.

The combined effect of absorption and scattering by different kinds of inhomogeneities in the media is referred to as media attenuation. The attenuation of sea bottom/sediments is generally given in unit dB per wavelength, indicating that the attenuation increases linearly with frequency. The sediment materials are three-to-four orders of magnitude more lossy than sea water [27]. Hence the effect of attenuation in sea water is negligible for the short propagation ranges often found in SAS applications. If the point scatterers lie in the water, the media attenuation loss can be estimated as $\beta_1(dr_1 + dr_2)/\lambda_1$ in dB. If the point scatterers lie in the bottom, the media attenuation loss along the rays in dB is given by $\beta_1(dr_1 + dr_4)/\lambda_1 + \beta_2(dr_2 + dr_3)/\lambda_2$. Loss-factors for an arbitrary number of frequencies are computed and stored for each ray. Hence, it is possible to model the distortion of the pulse due to the frequency-dependent attenuation loss. Approximations of the received signal are obtained by computing the attenuation loss factor for only one frequency, for example the center frequency of the transmitted pulse. In this case the received signal will be undistorted.

Since an interface between two homogeneous halfspaces is assumed, the transmission coefficients will be independent of frequency. The transmission coefficients T_{12} and T_{21} for transmission through the interface from halfspace 1 to 2 are given by,

$$T_{12} = \frac{2\frac{\rho_2 c_2}{cos(\theta_2)}}{\frac{\rho_2 c_2}{cos(\theta_2)} + \frac{\rho_1 c_1}{cos(\theta_1)}} \quad , \quad T_{21} = \frac{2\frac{\rho_1 c_1}{cos(\theta_4)}}{\frac{\rho_1 c_1}{cos(\theta_4)} + \frac{\rho_2 c_2}{cos(\theta_3)}} \quad , \tag{A.11}$$

where the incidence- and transmission angles θ_k are defined in Figure A.1.

The computation of the reflection loss at the point scatterers is at this stage not implemented and temporarily this loss factor is set to 1.

Rays that intersect one or more obstacles between the transmitter and the receiver give no, alternatively less, contribution to the received signal. If it is assumed that the obstacles are rigid, this loss factor will take either the value 0, i.e. the ray intersect an obstacles, or 1. If the obstacles are penetrable, the loss factor might take any value in the interval $[0, 1]$ instead. In this case the rays are also refracted when they penetrate the obstacle, why the simple ray structure with either 2 or 4 ray segments is not valid any longer. The computation of the shadow loss is at this stage not implemented.

Since the contributions along the rays are added coherently, the phase shifts due to surface reflections are important. In the present version of SASRAY the

number of surface reflections between a source and a point scatterer is limited to at most one, and allow at most one surface reflection also between the point scatterer and the receiver.

A.3 Source Pulse Generation

LFM pulses are often utilised in SAS. Consider a LFM pulse $p(t)$ as a function of time t,

$$p(t) = sin\left(2\pi\left(f_0 t + \frac{Bt^2}{2\tau_p}\right)\right) rect\left(\frac{t}{\tau_p}\right) , \tag{A.12}$$

where

$$f_0 = f_c - \frac{B}{2} , \tag{A.13}$$

and where f_c is the center frequency, B the bandwidth and τ_p the pulse length. In addition, the function $rect(t)$ is defined as,

$$rect(t) = \begin{cases} 1, \ 0 \leq t \leq \tau_p \\ 0, \ otherwise \end{cases} . \tag{A.14}$$

The instantaneous frequency is given by the time derivative of the phase of the LFM pulse,

$$f(t) = (f_0 + Bt/\tau_p)\, rect\left(\frac{t}{\tau_p}\right) . \tag{A.15}$$

If a LFM pulse is transmitted from the transmitter at time $t = 0$ the signal received at the receiver after propagation through the medium and reflection at a point scatterer is,

$$s(t) = p(t-T) = sin\left(2\pi\left(f_0(t-T) + \frac{B(t-T)^2}{2\tau_p}\right)\right) rect\left(\frac{t-T}{\tau_p}\right) , \tag{A.16}$$

where T is the traveltime from the transmitter to the point scatterer and back to the receiver. The sampled received signal at the receiver is then $x(n) = s(n/F_s)$, where F_s is the sampling frequency.

A.4 Target and Reverberation Models

The purpose of the target model is to provide tools for describing 3-D surfaces of generic objects such as spheres, boxes and cylinders. The surface of an object can then be discretized by point scatterers and used for calculating the combined reflected echoes of the target. For this purpose superellipsoids are suitable, see [28]. The bottom reverberation is also modeled by point scatterers, which are uniformly distributed at the seabed.

Thus, for each insonification of the target and the bottom all point scatterers will contribute to the total signal in each receiver element, where the amplitude of the source pulse (Section A.3) is adjusted according to ray trajectories (Section A.1) and when applicable ray losses mechanisms (Section A.2). Furthermore, the source pulse amplitudes of the point scatterers, modeling the bottom reverberation, are additionally adjusted to comply with a Weibull law [23]. This Weibull law is suitable for modeling the bottom reverberation speckle found in high-resolution SAS images. The probability density function $w_A(A)$ of the amplitude A of the Weibull law can be written as,

$$w_A(A) = \gamma^\zeta \zeta A^{\zeta-1} e^{-(\gamma A)^\zeta} , \tag{A.17}$$

where γ and ζ are constants which can be varied.

B Geoacoustic Parameters

In 2006 a field experiment [19] was carried out by FOI in the same area as the one considered in this report. An important object of the trial was to determine the geoacoustic properties of the upper sediment layers, since these are crucial for the ability of bottom penetrating SAS to detect buried objects.

Two rods were deployed vertically in the seabed. On each one of these, two hydrophones were mounted. The horizontal distance between the rods was 5 m, and the depths of the hydrophones were 30 and 60 cm respectively. An echo sounder (Airmar), located 10 m above the seabed and about 60 m from the hydrophone positions, was transmitting 10 ms long FM pulses. The beam width was 20° and the frequency range 20-30 kHz.

The recorded signals were to be matched by a 3-layer model of the bottom, where the bottommost third layer was prescribed to be postglacial clay with sound speed 1550 m/s, attenuation 0.2 dB/*wavelength* and density 1500 kg/m^3. The ray-tracing code RAYLAB [29] was used for modeling the wave propagation, and a global optimizer, differential evolution [30], searched the parameter space for an optimal combination of the seabed parameters. It turned out that the parameters of the second sediment layer could not be determined in this way. These were instead found from Topas data, see below. Furthermore, the densities of neither layer could be determined by this optimization approach, one instead has to rely on measurements of core samples from a nearby site.

The results indicate a sound speed of the uppermost sediment layer in the interval 1370-1390 m/s. This conforms well to the values obtained from direct measurements of the travel times when sending pulses between the hydrophones in the seabed (1360-1380 m/s), i.e. a sound speed of the uppermost layer well below the sound speed of the water. The absorption of this layer was found to be in the interval 0.03-0.06 dB/*wavelength*.

The thickness of the uppermost layer could not be well determined from these data because of the small difference in travel times between the direct and the reflected pulses with grazing angle below 10°. Instead, data from a mapping of the area around the hydrophones performed by the parametric sonar Topas 120, transmitting in the vertical direction, were used to compute the thickness from the travel times and the sediment sound speed determined above. This resulted in a thickness of the uppermost sediment layer of about 65 cm.

The thickness of the second sediment was determined from the Topas data in the same way. Because of lack of recorded sound speeds in this sediment, values obtained from core samples at a nearby site were used [6]. These indicate a sound speed of about 1500 m/s, resulting in a thickness of about 1 m. The densities were also found from the core samples, and were found to be about 1200-1350 kg/m^3 in the uppermost layer, and about 1300-1600 kg/m^3 in the second layer. The uncertainty in the density increases approaching the surface, due to possible occurrence of microgas in the sediment [31]. Therefore the density of the uppermost sediment layer might be overestimated in the core sample analysis.

C Equipment

One low frequency SAS and one high frequency SLS is mounted on the carriage. The low frequency sonar uses an Airmar M192 transmitter with the peak power located at a frequency of 24 kHz and a beam width of 20°. In the experiment the sonar is operated with LFM pulses from 20 to 30 kHz with pulse lengths of 20 ms. The pulses are generated by a WaveTek 395 Waveform Synthesizer, amplified by a bridged coupled Yamaha PC4800N amplifier and fed to the transmitter via a Krohn-Hite matching transformer model MT-56. The receiver is a linear antenna, made by Amlab Elektronik AB, Järfälla, Sweden. It has 16 elements with a spacing of 48 mm, which gives a lobe width of around 5° at 25 kHz. This low frequency sonar is intended for the detection of objects both below and above the sea bottom surface. Since the objects are quite close the transmitter is tilted 20° towards the bottom. The high frequency sonar is a Klein model 530T side looking sonar from Klein Associates Inc., USA. Its operating frequency is 340 kHz. The sonar tow-fish is stripped from its outer housing and fastened to the platform below the receiving array of the low frequency sonar. Only the right hand side hydrophone elements are used during the experiment. The carriage with low frequency SAS and the high frequency SLS is shown in figure C.1. By taking the trigger pulse and

Figure C.1: From top to bottom are seen, the Airmar M192 transmitter, the 16 element linear receiver, and the Klein 530T SLS mounted on the carriage.

the output from the detector it is possible to make digital recordings with a PC-based data acquisition system. Also the signals from the low frequency receiver are recorded by a similar system. Both systems are based on MicroStar Laboratories 14 bits analog-to-digital (A/D) converters together with FOI-developed software. Signals are low-pass filtered and sampled at 200 kHz per channel, and stored in disc files for subsequent analysis. The recording software

has facilities for data quality control, e.g. time series displays, spectral analysis and sidescan displays. Both recording computers are connected to a local area network with data back-up facilities and also another computer used for signal processing. In this way SAS processing in near real-time is possible.

D Test Site

The bedrock of the Stockholm Archipelago consists of crystalline granites, gneisses and leptites. Mostly the bedrock is covered by unconsolidated sediments which may be generalized as follows. Covering the bedrock is a thin layer of till, typically some meter thick. On top of the till are glacial and post-glacial clays deposited. Normally, the glacial clay is quite uniform in thickness being frequently a few meters thick. The glacial deposits are succeeded by post glacial clay and recent mud. The thickness of these latter sediments is highly variable due to local variations in conditions of accumulation and erosion. The post glacial sediment may reach several tens of meters in thickness.

The sea trial is performed at FOI:s research site Djupviken in the southern part of the Stockholm Archipelago. The water depth at the site is about 10 m. The seafloor consists of soft post glacial clay and mud, so called gyttja-clay, with an organic content of approximately 3 %. This is a rather inhomogeneous layer but with a persistent thickness of around 1.5 m in the area. The topmost layer is very soft with particles almost in suspension. This is most likely a result of the ordinary eroding swell of the shallower parts of the bay. The eroded particles are transported and deposited in deeper water as on the test site. The seabed surface is smooth and without any vegetation below the depth of a few meters, locally some minor structures a few cm in length are visible, Figure D.1. Acoustic in situ measurements in the uppermost part of

Figure D.1: The seafloor is fairly smooth; the visible small structures are a few centimetres long. In the upper left corner soft materials are suspended as the stand of the camera touches the seafloor.

the gyttja-clay indicate a velocity close to 1450 m/s [6]. Laboratory analyses of core samples show a bulk density just above 1500 kg/m^3 [32]. This will give

an impedance around $2.2 \cdot 10^6$ kg/m^{2}s, a value that can be expected for this type of sediment. On the other hand, earlier performed inversion modeling for the acoustic impedance has indicated values close to $1.6 \cdot 10^2$ kg/m^{2}s [31]. This discrepancy may be explained by the presence of gas in the uppermost sediment layer. The gas has disappeared from the retrieved cores but it influences the acoustic measurements performed at the location. Several other layers of unconsolidated sediments with a total thickness of some 3-4 m are underlying the mud layer and covering the crystalline bedrock.

The research site Djupviken includes a floating pontoon laboratory and an underwater rail. The rail is 13 m long and mounted on pillars at a height of 4 m above the seafloor, Figure D.2. The carriage with the two sonars is placed on top of the rail. The carriage is driven by an electric motor and remotely controlled from the pontoon laboratory and its position can be determined with sub-cm accuracy by reading a tape measure on the rail with an underwater camera.

Figure D.2: The rail, supported by tripods, before deployment.

FOI, Swedish Defence Research Agency, is a mainly assignment-funded agency under the Ministry of Defence. The core activities are research, method and technology development, as well as studies conducted in the interests of Swedish defence and the safety and security of society. The organisation employs approximately 1000 personnel of whom about 800 are scientists. This makes FOI Sweden's largest research institute. FOI gives its customers access to leading-edge expertise in a large number of fields such as security policy studies, defence and security related analyses, the assessment of various types of threat, systems for control and management of crises, protection against and management of hazardous substances, IT security and the potential offered by new sensors.

FOI
Defence Research Agency
Defence & Security, Systems and Technology
SE-164 90 Stockholm

Phone: +46 8 555 030 00
Fax: +46 8 555 031 00

www.foi.se